https://dx.doi.org/10.1016/j.compositesa.2021.106799

In situ Cure Monitoring and In-service Impact Localization of FRPs Using Pre-implanted Nanocomposite Sensors

Yiyin Su[a, §], Lei Xu[a, §], Pengyu Zhou[a], Jianwei Yang[a], Kai Wang[b], Li-min Zhou[c] and Zhongqing Su[a,d*]

[a]Department of Mechanical Engineering,
The Hong Kong Polytechnic University, Kowloon, Hong Kong SAR

[b]School of Aerospace Engineering,
Xiamen University, Xiamen, 361102, PR China

[c]School of System Design and Intelligent Manufacturing,
Southern University of Science and Technology, Shenzhen 518055, PR China

[d]The Hong Kong Polytechnic University Shenzhen Research Institute
Shenzhen, 518057, PR China

submitted to ***Composites Part A: Applied Science and Manufacturing***
(submitted on 24 Jul 2021; revised and resubmitted on 2nd Dec 2021)

§ These authors contributed equally to this work.
* To whom correspondence should be addressed. Tel.: +852-2766-7818, Fax: +852-2365-4703;
Email: zhongqing.su@polyu.edu.hk (Prof. Zhongqing Su, *Ph.D.*)

Abstract

From manufacturing onset through service, cure progress and structural integrity of fibre-reinforced polymer (FRP) composites are monitored continuously using a single type of pre-implanted nanocomposite sensors. The sensors precisely respond to broadband dynamic strains up to half a megahertz, yet without imposing intrusion to host composites and downgrading the original structural integrity. In conjunction with differential scanning calorimetry and a Sesták–Berggren autocatalytic kinetic model, cure behaviors of FRPs during fabrication are evaluated accurately, in terms of the matrix polymerization degree that is correlated with subtle changes in propagation characteristics of guided ultrasonic waves captured by the pre-implanted sensors. Use of the sensors is subsequently extended to structural integrity monitoring of FRPs that are in service. Experimental validation demonstrates that a transient impact to composites can be localized and imaged with the pre-implanted sensors. This study illustrates an *in situ* life cycle monitoring approach for FRPs using a single type of permanently implanted sensors with neglectable intrusion to composites.

***Keywords*:** A. Nanocomposites; D. Process monitoring; D. Ultrasonics; Structural health monitoring

1. Introduction

Real-time, continuous condition monitoring of fibre-reinforced polymer (FRP) composites, from the manufacturing onset, through service to the end of life, is of vital significance, to warrant structural integrity, reliability and durability spanning the entire life cycle of composites [1-3]. To accommodate such a need, prevailing approaches use multiple types of sensors with distinct sensing philosophies, to monitor different life cycle stages [1-3], yet the use of a single type of sensor for uninterrupted monitoring across multiple stages is increasingly attempted. As representative examples, Rufai *et al.* [4] and Nielsen *et al.* [5], respectively, developed optical fibre sensing networks to estimate strain accumulation in large-scale composites during manufacturing, and subsequently to measure strain variation using the same sensors when composites are subject to loadings in service. Notwithstanding, fibre optics-based sensors are of excessive thermal susceptibility to the ambient temperature fluctuation, restricted by which fibre optics-based sensors are usually used for monitoring cure progress of FRPs under an isothermal condition [6]. Contrast to this, optical fibres are, however, not sensitive to the presence of damage in FRPs that is distant, because such type of sensors can only perceive localized strain variation in sensor vicinity which is not remarkably affected by distant damage. The brittle nature of optical fibres entails extra caution during sensor embedding, adding extra complexity to FRP fabrication [7]. More importantly, optical fibres – a passive sensor, can only facilitate passive monitoring of strain changes in a relatively low-frequency regime.

Lead zirconate titanate (PZT)-made sensors respond to dynamic strains in a broad band, with proven sensing capability to entertain acousto-ultrasonics-based monitoring [8, 9]. PZT-type sensors can be immobilized with FRPs in either a surface-mounting or an internal-embedding manner, while the latter is preferred when isolation of sensors from

environmental attacks (*e.g.*, moisture and corrosion) or reliability of long-term signal acquisition is a concern. There is rich supply of approaches using embedded PZT wafers to implement cure monitoring or structural health monitoring (SHM) of FRPs [10, 11]. To name but a few, Liu *et al.* [10] evaluated the reaction progress of epoxy using embedded PZT wafers, and identified in-service damage in composites in terms of feature changes in guided ultrasonic waves (GUWs) captured by the same PZT wafers. This study endows conventional FRPs with the capacity of self-monitoring, in a continuous and promising manner. However, it is envisaged that when PZT-type sensors are embedded in FRPs, these sensors downgrade, to a certain degree, the composites' original structural integrity [12, 13]. To put it into perspective [13], the reduction in flexural and compression strengths of a FRP, due to the embedment of a PZT wafer, can be as high as 8% and 12%, respectively.

Recent advances in nanomaterials have offered new possibility to revamp the monitoring philosophy of FRPs through a life cycle, with minimized intrusion to composites due to sensor embedment [14-16]. Luo *et al.* [17, 18] decorated glass fibres with carbonaceous nanomaterials to calibrate the impedance of glass fibre-reinforced polymer composites, on which basis the polymer cure progress was evaluated. The cure monitoring was followed with failure prediction using the same developed fibre sensors when the composites were loaded. In addition to the above fibre sensors, Wang *et al.* [19] and Wang *et al.* [20] respectively developed a laser-induced graphene-based sensor which can be integrated in composites to perform through-life monitoring of structural integrity, with additional merits such as fire retardancy and the function of de-icing. In a similar vein, Lu *et al.* [21] and Ali *et al.* [22] also, respectively, demonstrated the efficiency of using buckypaper and graphene-coated fabrics for process monitoring via measuring the variation in electrical

resistance. The principle of both cure evaluation in fabrication and integrity monitoring in service was based on the premise that the change in resin consolidation or the occurrence of damage alters the electrical resistance measured by the nanomaterial-based sensors. Prevailing approaches in this category are limited to the use of polymer composites with dielectric reinforcements (*e.g.*, glass, aramid or nylon fibres), in which short-circuit of sensors by fibres is not an issue. In addition, electrical resistance is a global parameter, only qualitatively and holistically reflecting the alteration in material properties between a pair of electrodes. Though several studies [23, 24] have demonstrated that the electrical impedance tomography is an efficient monitoring approach, the sensitivity of such a technique, when it is used for quantitative evaluation of micro-scale damage, still needs further proof.

In contrast to electrical impedance, GUWs of higher frequencies carry fairly localized information that is accumulated along wave propagation paths, able to quantitatively estimate cure progress (during manufacturing) or integrity degradation due to damage (in service) even if the damage is distant from the sensor or of microscale [25, 26]. As commented earlier, conventional GUW-based monitoring is regularly implemented in conjunction with the use of PZT-type sensors for GUW generation and acquisition, embedment of which unavoidably degrades the original structural integrity of host composites. On the other hand, the majority of nanocomposite/nanomaterial-based sensors are engineered to perceive quasi-static or low-frequency cyclic strains [27]. He *et al.* [28] recently reported a new genre of one-dimensional, graphene-enabled fibre electronic, which can faithfully capture ultrasonic signals of the frequency up to ~20 kHz. However, there is still limited endeavor to develop implantable sensors that are able to respond to GUWs of several hundred kilohertz or even megahertz.

In such a backdrop, we expand our continued endeavour in developing nano-engineered sensors for GUW-based SHM [29-32]. A genre of nanocomposite sensors is tailor-made, to respond to GUWs of half a megahertz. The sensors are pre-implanted in FRPs, with which cure progress calibration during manufacturing and integrity monitoring in service of FRPs are hierarchically implemented, by scrutinizing subtle changes in propagation characteristics of GUWs perceived by the sensors. With differential scanning calorimetry (DSC) and a Sesták–Berggren autocatalytic kinetic model, cure behaviors of composites are evaluated continuously, in terms of the matrix polymerization, to different degree of which GUWs manifest various propagation traits. Use of the pre-implanted sensors is subsequently expanded to structural integrity monitoring, in which a transient impact to composites is localized and imaged. GUW-based continuous monitoring of FRPs spanning from manufacturing to service, in a real-time and *in situ* manner, is achieved using a single type of permanently implanted sensors, yet without sacrificing the original structural integrity of host FRPs.

2. Cure Kinetics of Matrix

Material properties of FRPs (*e.g.*, stiffness and strength) are associated with the cure degree of matrix in a curing process [33]. On the other hand, propagation attributes of GUWs in FRPs are also dependent on material properties (*e.g.*, density and stiffness) and geometric features of FRPs [34]. Provided that the density and geometric features of a FRP, and the properties of fibres remain unchanged through the curing process [8, 35], the change in propagation characteristics of GUWs can reflect the cure information of matrix.

To develop such a correlation, cure behaviors of FRPs are first investigated via DSC and a Sesták–Berggren autocatalytic kinetic model. Without loss of generality, a unidirectional

144 E-glass epoxy prepreg (Guangwei Composites® G15000; thickness: 0.15 mm; fibre weight:
145 150 gsm; resin content: ~40 wt.%) is characterized with a differential scanning calorimeter
146 (METTLER TOLEDO® DSC 3) in a nitrogen atmosphere (20 sccm) at the heating rate (β
147) of 1.0, 1.5, 2.0, 3.0, and 4.5 K/min, respectively, in a temperature range from 298.15 to
148 523.15 K. Prepreg sample (~2 mg) is sealed in an aluminum DSC pan, and placed in the
149 DSC chamber, along with another empty DSC pan that is heated simultaneously for
150 benchmarking.
151
152 The DSC curves (*viz.*, heat flow *vs.* heating temperature) of the prepreg, representing the
153 cure progress of matrix, obtained at representative heating rates, are compared in **Fig. 1**, in
154 which an exothermic peak is observed in each curve. As β increases, the exothermic peak
155 shifts to a higher temperature range with a higher magnitude of exotherm, which is
156 attributable to a higher increasing rate of the temperature.
157
158 With results in **Fig. 1**, the cure degree against time, $\alpha(t)$, is defined as
159 $$\alpha(t) = \frac{H(t)}{H_T}, \quad \textbf{(1)}$$
160 where $H(t)$ is the reaction enthalpy released till a moment of investigation t; H_T signifies
161 the total reaction enthalpy which is to be obtained by integrating the heat flow over the
162 entire exothermic peak area in **Fig. 1**.
163
164 The cure rate, $\frac{d\alpha(t)}{dt}$, can be correlated to the ambient temperature T through curing [36,
165 37] as
166 $$\frac{d\alpha(t)}{dt} = k(T) \cdot f(\alpha), \quad \textbf{(2)}$$

where $k(T)$ denotes a temperature-dependent constant, and $f(\alpha)$ the function representing a kinetic model (to be detailed in the sequent section). $k(T)$ can be expressed using an Arrhenius equation [38] as

$$k(T) = A \cdot e^{\frac{-E}{RT}}, \quad \textbf{(3)}$$

where A represents a pre-exponential factor, E the apparent activation energy, and R the universal gas constant (8.314 J·mol^{-1}·K^{-1}). With above correlations, **Eq. (2)** can be re-written as

$$\frac{d\alpha(t)}{dT} = \frac{A}{\beta} \cdot e^{\frac{-E}{RT}} f(\alpha). \quad \textbf{(4)}$$

To estimate E and A, the Kissinger method [38, 39] is recalled. The method assumes that the cure degree of resin, regardless of β, remains the same when $\frac{d\alpha(t)}{dt}$ reaches its maximum, on which basis one has

$$\ln(\frac{\beta}{T_p^2}) = \ln(\frac{AR}{E}) - \frac{E}{RT_p}, \quad \textbf{(5)}$$

where T_p is the temperature, at which $\frac{d\alpha(t)}{dt}$ reaches its maximum at a given β. Via plotting $\ln(\beta/T_p^2)$ versus $1/T_p$, calculating the slope of linear fit and determining the y-intercept, the values of E and $\ln A$ are obtained as 86.26 kJ/mol and 24.87 ln(min^{-1}), respectively, as shown in **Fig. 2(a)**.

With known E and $\ln A$, the Sesták–Berggren model [37-39] is applied, in conjunction with the obtained DSC results in **Fig. 1**, to ascertain $f(\alpha)$. With the Sesták–Berggren model, $f(\alpha)$ is approximated by

$$f(\alpha) = \alpha(t)^m (1-\alpha(t))^n, \quad \textbf{(6)}$$

where *m* and *n* are two unknown variables to be determined. Substituting **Eqs. (6)** into **(4)** and taking the logarithm of the equation, it yields

$$\ln\left(\frac{d\alpha(t)}{dt}e^{\frac{E}{RT}}\right) = n\cdot\ln[\alpha(t)^p(1-\alpha(t))] + \ln A, \quad \textbf{(7)}$$

where $p = \frac{m}{n}$. On the other hand, introducing $\alpha(t)_M$ which represents the cure degree, at which $\frac{d\alpha(t)}{dt}e^{\frac{E}{RT}}$ reaches its maxima at a given β (as indicated in **Fig. 2(b)**), p can be calculated via

$$p = \frac{\alpha(t)_M}{1-\alpha(t)_M}. \quad \textbf{(8)}$$

In **Fig. 2(b)**, it can be seen that for all β of investigation, $\alpha(t)_M$ remains a constant of ~0.3, and p is therefore ~0.43. With it, *n* and *m* are further calculated, in **Table 1**. With all parameters in **Table 1**, the correlation between $\frac{d\alpha(t)}{dt}$ and cure temperature, and the correlation between $\alpha(t)$ and cure temperature are fitted with the Sesták–Berggren model, and shown in **Fig. 3**. These two correlations can be extended to calculate the cure rate ($\frac{d\alpha(t)}{dt}$), and the cure degree ($\alpha(t)$) against the cure temperature, at a given heating rate (β).

On the other hand, different cure degrees of matrix modulate propagation characteristics of GUWs in FRPs distinctly. Facilitated by the correlations in **Fig. 3**, $\alpha(t)$ can thus be linked to the group velocity (C_g) of GUWs, by taking into account different heating rates (β). With measured C_g, the cure degree can be evaluated (in **Section 3.2**).

3. Continuous Monitoring of Cure Progress and Structural Integrity

By virtue of the cure kinetic model and the correlation between GUW features and cure degree, monitoring of cure progress of FRPs during manufacturing and structural integrity in service is implemented continuously and hierarchically, using pre-implanted nanocomposite sensors.

3.1 Fabrication of Implantable Nanocomposite Sensors

A new sort of piezoresistive nanocomposite sensors is developed via spray coating – a cost-effective additive manufacturing approach. To prepare the sprayable nanocomposite ink, graphene nanoplatelets (GNPs) (TANFENG®; thickness: ~1 nm; diameter: ~50 μm; SSA: ~1200 m^2/g; and purity: >99 wt.%) and polyvinylpyrrolidone (PVP) (Sigma-Aldrich® PVP K-30) are dissolved in 20 ml ethanol, at a weight ratio of 1:19 (0.05 g and 0.95 g, respectively). The sensors, with a planar dimension of 20 × 3 mm^2 each, are deposited on a partially pre-cured B-stage epoxy film using an airbrush. The epoxy film is pre-cured to achieve the cure degree of ~0.4, so that possible flowing of epoxy can be restrained, and the initial morphology of nanocomposite ink deposited on the film can be remained. To minimize intrusion to host FRPs, the sensors are electrified using highly conductive carbon nanotube film (CNT-film)-made wires (DexMat®; linear resistance: 20±3 Ω/m; thickness: 10±5 μm; width: 1±0.1 mm). Another layer of epoxy film is placed on the sensors and CNT-film-made wires. Both epoxy films, respectively atop and beneath the sensors and wires, work as a pair of dielectric membranes to encapsulate the sensors and insulate them from conductive fibres (*e.g.*, carbon fibre) when implanted into FRPs. The encapsulated sensors are entirely cured under a vacuum-assisted cure condition (130 ℃, 60 min). A batch of finished sensors is photographed in **Fig. 4**. Scanning electron microscopy (SEM) images of a sensor are shown in **Fig. 5**. In **Fig. 5(a)**, the thickness of

sensor including its wires is measured to be ~45 μm only; in **Fig. 5(b)**, GNPs are observed to disperse in PVP matrix evenly – a critical merit to enhance the sensitivity of piezoresistive sensors to high-frequency dynamic strains (*e.g.*, GUWs).

To interrogate the possible intrusion of implanted sensors to the host FRP composites, sensors are implanted between the 4^{th} and 5^{th} plies of an eight-ply quasi-isotropic $[0/90/45/-45]_s$ FRP laminate, which is then cured in accordance with a standard autoclaving process with key parameters listed in **Table S1**. Tensile and bending tests, in accordance with ASTM D3039 and D790 respectively, are conducted to gauge the degradation in mechanical attributes of FRPs due to sensor intrusion. For each category of test, three FRP specimens, each of which is implanted with a nanocomposite sensor, along with another three specimens which are of the same dimensions but without sensor implantation, are tested. **Figure S1** displays the mechanical test results of FRPs with and without the implanted sensor. Both the stress-strain curves (acquired in the tensile test) and the load-displacement curves (acquired in the bending test) demonstrate that the implanted sensor does not result in measurable degradation in elastic attributes of the host composites, before the specimen fracture. Neglectable change in tensile and flexural strengths is observed: the tensile strength decreases slightly from its original 845.9±15.38 MPa to 823.5±17.41 MPa upon implantation of sensors, and the flexural strength increases marginally from 916.6±30.35 MPa to 950.9±67.49 MPa (the slight increase is attributable to the discrepancy among tested specimens). **Figure 6** shows the cross-section of laminate with an implanted sensor (including its CNT-film-made wires), insert of which highlights the sensor vicinity and accentuates the excellent interface between prepreg and sensor. The mechanical test results have demonstrated the high compatibility of the implanted sensors with the host composites.

Responsivity of the implanted sensors to quasi-static tensile loads and high-frequency GUWs is respectively calibrated (detailed experimental configuration in **Section 3.2.1**). The nanocomposite sensors, by virtue of the quantum tunnelling effect [40, 41], demonstrate sufficient sensitivity to dynamic strains in a broad band, ranging from static tensile loads (with a gauge factor of 34.5), as shown in **Fig. S2(a)**, to GUWs up to 450 kHz, in **Figs. S2(b)** and **(c)**.

3.2 Cure Monitoring

With the Sesták–Berggren model, the matrix cure degree ($\alpha(t)$) is correlated with group velocity (C_g) of GUWs perceived by the pre-implanted sensors, and the cure progress of FRPs can be monitored in a real-time and *in situ* manner.

3.2.1 Methodology

Eight plies of unidirectional E-glass epoxy prepregs are stacked to produce an 8-layer quasi-isotropic $[0/90/45/-45]_s$ FRP laminate ($500 \times 500 \times 1.15$ mm^3). A group of eight nanocomposite sensors is implanted between the 4th and 5th prepregs, to configure a sparse sensor network via CNT-film-made wires. The sensor network is instrumented with a self-developed signal generation and acquisition system, as illustrated schematically in **Fig. 7**. Two ETFE peel films (AIRTECH® WL5200B), 15 μm thick each, are placed atop and beneath the stacked prepregs. The stacked prepregs that are sandwiched by the peel films are placed on an aluminium tooling plate covered with a layer of thick breather. A miniaturized PZT wafer (PSN-33; Ø: 12 mm; 1 mm thick) is surface-placed at the centre of the upper peel film for GUW generation, which is 150 mm from each of the eight nanocomposite sensors. Under the vacuum pressure of -25 inHg, a good acoustic coupling is achieved between the PZT wafer and prepregs, warranting efficient generation and

transmission of GUWs. After adding another thick breather layer on the upper peel film, the prepregs undergo a standard vacuuming process. Upon vacuuming, prepregs are heated from 298.15 to 458.15 K until the laminate is fully cured.

A 5-cycle Hanning-function-modulated sinusoidal toneburst is generated at a frequency of 175 kHz every ten microseconds, using a waveform generator on NI® PXIe-1071 platform. The generated signal is applied on the PZT wafer, after it is amplified to 400 V_{p-p} via a linear power amplifier (Ciprian® US-TXP-3). Propagation of the generated GUWs in prepregs during the cure progress is perceived with the pre-implanted sensors and recorded with an oscilloscope (Agilent® DSO9064A), as shown in **Fig. 7**.

3.2.2 Results

All GUW signals recorded as cure progresses are applied with a first-order Butterworth filter to mitigate ambient noise and measurement uncertainties. **Figure 8** shows representative GUW signals perceived by a pre-implanted sensor, along with the energy envelopes of signals obtained via the Hilbert transform, at different temperatures with the heating rate of 1.5 K/min. The Hilbert transform is an approach to canvass a signal in the time domain in terms of its energy distribution, and the envelope depicts the signal energy migration against time. It can be seen in **Fig. 8** that both the group velocity of GUWs and signal amplitudes change remarkably against temperature through curing.

The group velocity of the zeroth-order symmetric Lamb wave mode (denoted by S_0 in figures) is extracted from signals, with which the cure progress of matrix is real-time monitored according to the Sesták–Berggren model. C_g is calculated in virtue of the time at which the signal energy envelope reaches its peak, as

$$C_g = \frac{L}{t_s - t_e}, \quad \textbf{(9)}$$

where L (150 mm) is the distance between the PZT wafer and a nanocomposite sensor. t_e and t_s signify the moments, at which the energy envelope reaches its peak, respectively for the excitation signal and for the sensor-received signal.

A batch of 8-layer prepregs, each with the pre-implanted nanocomposite sensor network and a surface-placed PZT wafer, is prepared. As representative results, for each heating rate (namely 1.0 and 1.5 K/min), two groups of measured signals are displayed in **Fig. 9**, showing the progressive alteration in C_g of the S_0 wave mode through a curing process. The S_0 wave mode is measurable at the beginning of cure. As observed, C_g of the S_0 wave mode decreases, as the cure temperature elevates, until wave signals can no longer be identified due to the fact that the matrix becomes a highly attenuative, viscous liquid; as cure continues, the S_0 wave mode is measurable again from ~393 K for the heating rate of 1.0 K/min, and from ~399 K for 1.5 K/min, at which the corresponding cure degrees are 0.620 (for 1.0 K/min) and 0.625 (for 1.5 K/min), as predicted by the Sesták–Berggren model. These results are consistent with the cure degree at the gel point of the matrix (~0.6) as provided by the manufacturer. As depicted in **Fig. 9**, after the gel point of matrix, C_g of GUWs increases rapidly, as a result of a higher crosslinking density of the resin. The increasing rate of C_g decreases after the matrix begins its vitrification and subsequently remains slight change which indicates the completion of cure.

The alteration of C_g of the S_0 wave mode is quantitatively associated with the change in stiffness of the matrix which reflects the cure degree, as shown in **Fig. 10**. In **Fig. 10(a)**, good consistence among all experimentally measured C_g is noted when the cure degree of

matrix is the same, irrespective of different heating rates. With **Fig. 10(a)**, the correlation between the cure degree of matrix and C_g of the S_0 wave mode is fitted as

$$C_g = 1035\int_{0.625}^{\alpha} \alpha^{0.39}(1-\alpha)^{0.26} d\alpha + 2460, \quad \textbf{(10)}$$

as shown in **Fig. 10(b)**. With such a correlation, cure information of composites after the gel point of matrix can be monitored in a real-time manner with the pre-implanted nanocomposite sensors, to quantify the cure degree of matrix and indicate the completion of resin cure.

3.2.3 Cure Anomaly Detection

With **Eq. (10)**, the cure progress of another two sets of 8-layer prepregs is monitored at the heating rate of 2.0 K/min. To introduce a mock-up anomaly in a curing process, a heating tape (measuring 15 × 3 cm^2) is adhered at the back surface of the tooling plate for one of the two sets. The tape is located along the GUW propagation path that is linked by the PZT wafer and the nanocomposite sensor I (indicated in **Fig. S3**). The heating tape quickly elevates the temperature of matrix in the vicinity of tape, at a higher heating rate than that in the rest region of matrix. A thermocouple is collocated alongside the tape to real-time record the temperature change in such an abnormal heating area. As seen in **Fig. 11(a)**, the predicted C_g, obtained via the Sesták–Berggren model and also **Eq. (10)**, is consistent with that experimentally measured in the normal heating area of matrix; in contrast, the C_g measured from the abnormal heating area shows inconsistence with the model-predicted C_g, in **Fig. 11(b)**, implying cure anomaly.

3.3 In-service Impact Localization

Subsequent to the above cure progress monitoring, structural integrity of the same FRP laminate in service is further evaluated, using the same pre-implanted nanocomposite sensor network. The eight nanocomposite sensors in the network are denoted with S_i ($i = 1, 2, \mathrm{L}\ , 8$), enclosing a circular inspection area with a radius of 150 mm, **Fig. 7**. As a proof-of-concept validation, a steel ball (Ø: 8 mm; weight: 10 g) impinges on the laminate from a height of 250 mm (~25×10^{-3} J impact energy) in a drop-weight impact test, and the impact triggers acoustic emission (AE) signals that are captured by the sensors and recorded with the system. Raw signals are applied with a first-order Butterworth low-pass filter with the cut-off frequency of 10 kHz, to supress measurement noise. A delay-and-sum triangulation algorithm [42] is recalled to image the impact spot. In the algorithm, the moment t_i, at which the first-arrival wave component is captured with the i^{th} sensor located at (x_i, y_i), is defined as

$$t_i = t_0 + \Delta t_i\,, \tag{11}$$

where t_0 denotes the moment at which the steel ball impinges on the laminate, and Δt_i the time for the first-arrival wave component in the AE signal to travel from the impact spot to S_i. With another sensor S_j at (x_j, y_j), the difference (*i.e.*, $\Delta t_{ij}(x, y)$) in the arrival time of AE signals captured by S_i and S_j reads

$$\Delta t_{ij}(x, y) = t_i - t_j = (t_0 + \Delta t_i) - (t_0 + \Delta t_j) = \frac{\sqrt{(x - x_i)^2 + (y - y_i)^2} - \sqrt{(x - x_j)^2 + (y - y_j)^2}}{v_{plate}}, \tag{12}$$

$$(i = 1, 2, \mathrm{L}\ , 8)$$

where variables are distinguished by subscripts i and j for two individual sensors, v_{plate} the velocity of the first-arrival wave component, and (x, y) the impact spot location. A two-

dimensional grey-scale image is obtained using the delay-and-sum triangulation algorithm, in which each pixel value ($\xi_{ij}(x, y)$) is defined as

$$\xi_{ij}(x, y) = \max(E_i + E_j(\Delta t_{ij}(x, y))), \quad \textbf{(13)}$$

where E is the energy packet of the first-arrival wave component extracted from the AE signals. The max operator in the equation defines the maximal of summation of two signals received by S_i and S_j, which is associated with the probability of impact spot – that is the perception as to the impact spot from the perspective of the sensor pair of S_i and S_j. Aggregating images constructed by all sensor pairs rendered by the sensor network, a superimposed image is made, in which those pixels with greater values have a higher degree of probability of the impact spot, and *vice versa*. **Figures 12(a)** and **(b)** show the raw and filtered signals captured by S_3 and S_5, as an example; **Fig. 12(c)** highlights the identified impact location using the above delay-and-sum algorithm, in which the colour gradient calibrates the probability of the occurrence of an impact. A high degree of coincidence between the identified impact spot and reality is observed.

4. Concluding Remarks

This study demonstrates a new approach for *in situ*, online monitoring of FRPs using a new kind of implantable nanocomposite sensors, from cure monitoring to in-service impact localization. The pre-implanted sensors, fabricated by spray coating the GNPs/PVP nanocomposite ink on partially pre-cured B-stage epoxy films, are ~45 μm in thickness and demonstrate nonintrusive attributes with the host FRPs, resulting neglectable variation in both tensile (<3%) and flexural (<4%) strengths. Being capable of perceiving strains in a broad frequency range from quasi-static loads (with a high gauge factor of 34.5) to GUWs up to 450 kHz, the sensors endow conventional composites with a capability to self-

monitor the matrix cure progress and self-detect the cure anomaly, if any, via interpreting subtle changes in propagation characteristics of sensor-captured GUW signals. The use of the same type of sensors can also be extended to structural integrity evaluation of FRPs when the composites are in service, as proven by the experimental validation.

Acknowledgments

The work was supported by General Project (Nos. 51875492 and 12072141) and a Key Project (No. 51635008) received from the National Natural Science Foundation of China. Z Su acknowledges the support from the Hong Kong Research Grants Council via General Research Funds (Nos. 15202820, 15204419 and 15212417).

References

[1] Sandberg M, Yuksel O, Baran I, Hattel JH, Spangenberg J. Numerical and experimental analysis of resin-flow, heat-transfer, and cure in a resin-injection pultrusion process. Compos Part A Appl Sci Manuf 2020;143:106231.

[2] Hwang S, Jeon I, Han G, Sohn H, Yun W. Visualization and classification of hidden defects in triplex composites used in LNG carriers by active thermography. Smart Struct Syst 2019;24(6):803-12.

[3] Zhang Z, Liu M, Li Q, Png M. Baseline-free defect evaluation of complex-microstructure composites using frequency-dependent ultrasound reflections. Compos Part A Appl Sci Manuf 2020;139:106090.

[4] Rufai O, Chandarana N, Gautam M, Potluri P, Gresil M. Cure monitoring and structural health monitoring of composites using micro-braided distributed optical fibre. Compos Struct 2020;254:112861.

[5] Nielsen MW, Schmidt JW, Høgh JH, Waldbjørn JP, Hattel JH, Andersen TL, *et al*. Life cycle strain monitoring in glass fibre reinforced polymer laminates using embedded fibre Bragg grating sensors from manufacturing to failure. J Compos Mater 2014;48(3):365-81.

[6] Nair AK, Machavaram VR, Mahendran RS, Pandita SD, Paget C, Barrow C, *et al*. Process monitoring of fibre reinforced composites using a multi-measurand fibre-optic sensor. Sens Actuators B Chem 2015;212:93-106.

[7] Qing X, Liu X, Zhu J, Wang Y. In-situ monitoring of liquid composite molding process using piezoelectric sensor network. Struct Health Monit 2020:1475921720958082.

[8] Mizukami K, Yoshimoto S, Ogi K. In-process acquisition of cure-dependent viscoelastic properties of carbon fiber reinforced composites using micromechanics-based guided wave analysis. Polym Test 2018;65:459-67.

[9] Xu L, Su Y, Wang K, Yang X, Yuan S, Su Z. An Elastodynamic Reciprocity Theorem-based Closed-form Solution to Second Harmonic Generation of Lamb Waves by A Fatigue Crack: Theory & Experimental Validation. J Sound Vib 2021;509:116226.
[10] Liu X, Li J, Zhu J, Wang Y, Qing X. Cure monitoring and damage identification of CFRP using embedded piezoelectric sensors network. Ultrasonics 2021;115:106470.
[11] Su Z, Wang X, Chen Z, Ye L, Wang D. A built-in active sensor network for health monitoring of composite structures. Smart Mater Struct 2006;15(6):1939.
[12] Konka HP, Wahab M, Lian K. The effects of embedded piezoelectric fiber composite sensors on the structural integrity of glass-fiber–epoxy composite laminate. Smart Mater Struct 2011;21(1):015016.
[13] Andreades C, Mahmoodi P, Ciampa F. Characterisation of smart CFRP composites with embedded PZT transducers for nonlinear ultrasonic applications. Compos Struct 2018;206:456-66.
[14] Li W, He D, Bai J. The influence of nano/micro hybrid structure on the mechanical and self-sensing properties of carbon nanotube-microparticle reinforced epoxy matrix composite. Compos Part A Appl Sci Manuf 2013;54:28-36.
[15] Li W, He D, Dang Z, Bai J. In situ damage sensing in the glass fabric reinforced epoxy composites containing CNT–Al2O3 hybrids. Compos Sci Technol 2014;99:8-14.
[16] Su Y, Xu L, Zhou P, Yang J, Wang K, Zhou L-m, *et al*. Carbon nanotube-decorated glass fibre bundles for cure self-monitoring and load self-sensing of FRPs. Compos Commun 2021;27:100899.
[17] Luo S, Liu T. Graphite nanoplatelet enabled embeddable fiber sensor for in situ curing monitoring and structural health monitoring of polymeric composites. ACS Appl Mater Interfaces 2014;6(12):9314-20.
[18] Luo S, Obitayo W, Liu T. SWCNT-thin-film-enabled fiber sensors for lifelong structural health monitoring of polymeric composites-From manufacturing to utilization to failure. Carbon 2014;76:321-9.
[19] Wang Y, Wang Y, Zhang P, Liu F, Luo S. Laser-Induced Freestanding Graphene Papers: A New Route of Scalable Fabrication with Tunable Morphologies and Properties for Multifunctional Devices and Structures. Small 2018;14(36):1802350.
[20] Wang G, Wang Y, Luo Y, Luo S. A self-converted strategy toward multifunctional composites with laser-induced graphitic structures. Compos Sci Technol 2020;199:108334.
[21] Lu S, Chen D, Wang X, Shao J, Ma K, Zhang L, *et al*. Real-time cure behaviour monitoring of polymer composites using a highly flexible and sensitive CNT buckypaper sensor. Compos Sci Technol 2017;152:181-9.
[22] Ali MA, Umer R, Khan KA, Samad YA, Liao K, Cantwell W. Graphene coated piezo-resistive fabrics for liquid composite molding process monitoring. Compos Sci Technol 2017;148:106-14.
[23] Dai H, Thostenson ET. Scalable and multifunctional carbon nanotube-based textile as distributed sensors for flow and cure monitoring. Carbon 2020;164:28-41.
[24] Tallman TN, Gungor S, Wang K, Bakis CE. Damage detection via electrical impedance tomography in glass fiber/epoxy laminates with carbon black filler. Struct Health Monit 2015;14(1):100-9.
[25] Ren Y, Qiu L, Yuan S, Su Z. A diagnostic imaging approach for online characterization of multi-impact in aircraft composite structures based on a scanning spatial-wavenumber filter of guided wave. Mech Syst Signal Process 2017;90:44-63.
[26] Zhang Z, Liu M, Liao Y, Su Z, Xiao Y. Contact acoustic nonlinearity (CAN)-based continuous monitoring of bolt loosening: Hybrid use of high-order harmonics and spectral sidebands. Mech Syst Signal Process 2018;103:280-94.

[27] Zeng Z, Liu M, Xu H, Liao Y, Duan F, Zhou L-m, *et al*. Ultra-broadband frequency responsive sensor based on lightweight and flexible carbon nanostructured polymeric nanocomposites. Carbon 2017;121:490-501.
[28] He M, Wang Y, Wang S, Luo S. Laser-induced graphene enabled 1D fiber electronics. Carbon 2020;168:308-18.
[29] Zhou P, Yang X, Su Y, Yang J, Xu L, Wang K, *et al*. Direct-write nanocomposite sensor array for ultrasonic imaging of composites. Compos Commun 2021;28:100937.
[30] Zhou P, Liao Y, Yang X, Su Y, Yang J, Xu L, *et al*. Thermally stable, adhesively strong graphene/polyimide films for inkjet printing ultrasound sensors. Carbon 2021;184:64-71.
[31] Li Y, Wang K, Wang Q, Yang J, Zhou P, Su Y, *et al*. Acousto-ultrasonics-based health monitoring for nano-engineered composites using a dispersive graphene-networked sensing system. Struct Health Monit 2021;20(1):240-54.
[32] Zhou P, Liao Y, Li Y, Pan D, Cao W, Yang X, *et al*. An inkjet-printed, flexible, ultra-broadband nanocomposite film sensor for in-situ acquisition of high-frequency dynamic strains. Compos Part A Appl Sci Manuf 2019;125:105554.
[33] Ghodhbani N, Maréchal P, Duflo H. Ultrasound monitoring of the cure kinetics of an epoxy resin: Identification, frequency and temperature dependence. Polym Test 2016;56:156-66.
[34] Su Z, Ye L, Lu Y. Guided Lamb waves for identification of damage in composite structures: A review. J Sound Vib 2006;295(3-5):753-80.
[35] Mizukami K, Ikeda T, Ogi K. Measurement of velocity and attenuation of ultrasonic guided wave for real-time estimation of cure-dependent anisotropic viscoelastic properties of carbon fiber-reinforced plastics. Ultrasonics 2019;99:105952.
[36] Huang X, Patham B. Experimental characterization of a curing thermoset epoxy-anhydride system—Isothermal and nonisothermal cure kinetics. J Appl Polym Sci 2013;127(3):1959-66.
[37] Yoo MJ, Kim SH, Park SD, Lee WS, Sun J-W, Choi J-H, *et al*. Investigation of curing kinetics of various cycloaliphatic epoxy resins using dynamic thermal analysis. Eur Polym J 2010;46(5):1158-62.
[38] Hayaty M, Beheshty MH, Esfandeh M. Cure kinetics of a glass/epoxy prepreg by dynamic differential scanning calorimetry. J Appl Polym Sci 2011;120(1):62-9.
[39] Roşu D, Caşcaval C, Mustăţă F, Ciobanu C. Cure kinetics of epoxy resins studied by non-isothermal DSC data. Thermochim Acta 2002;383(1-2):119-27.
[40] Liao Y, Duan F, Zhang H, Lu Y, Zeng Z, Liu M, *et al*. Ultrafast response of spray-on nanocomposite piezoresistive sensors to broadband ultrasound. Carbon 2019;143:743-51.
[41] Hu N, Karube Y, Yan C, Masuda Z, Fukunaga H. Tunneling effect in a polymer/carbon nanotube nanocomposite strain sensor. Acta Mater 2008;56(13):2929-36.
[42] Liu M, Zeng Z, Xu H, Liao Y, Zhou L, Zhang Z, *et al*. Applications of a nanocomposite-inspired in-situ broadband ultrasonic sensor to acousto-ultrasonics-based passive and active structural health monitoring. Ultrasonics 2017;78:166-74.

Figures

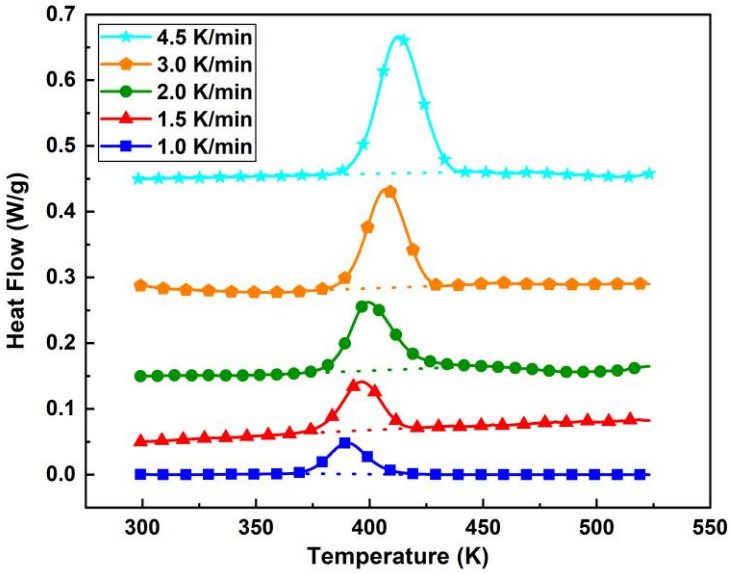

Fig. 1. DSC curves of prepregs at the heating rate of 1.0, 1.5, 2.0, 3.0, and 4.5 K/min, respectively.

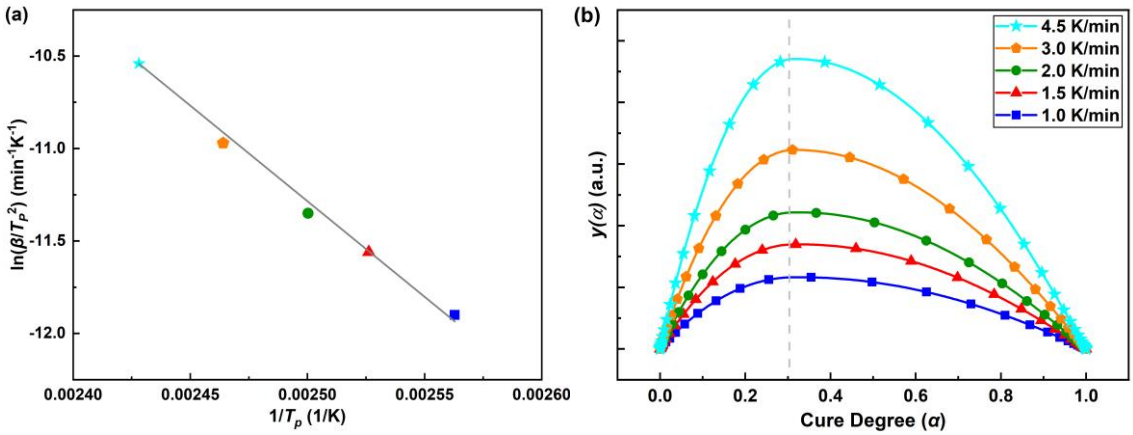

Fig. 2. (a) Kissinger plot for determining E and ln$A$; and (b) plot of $y(\alpha)=\frac{d\alpha(t)}{dt}e^{\frac{E}{RT}}$ *versus* cure degree ($\alpha(t)$) at different β.

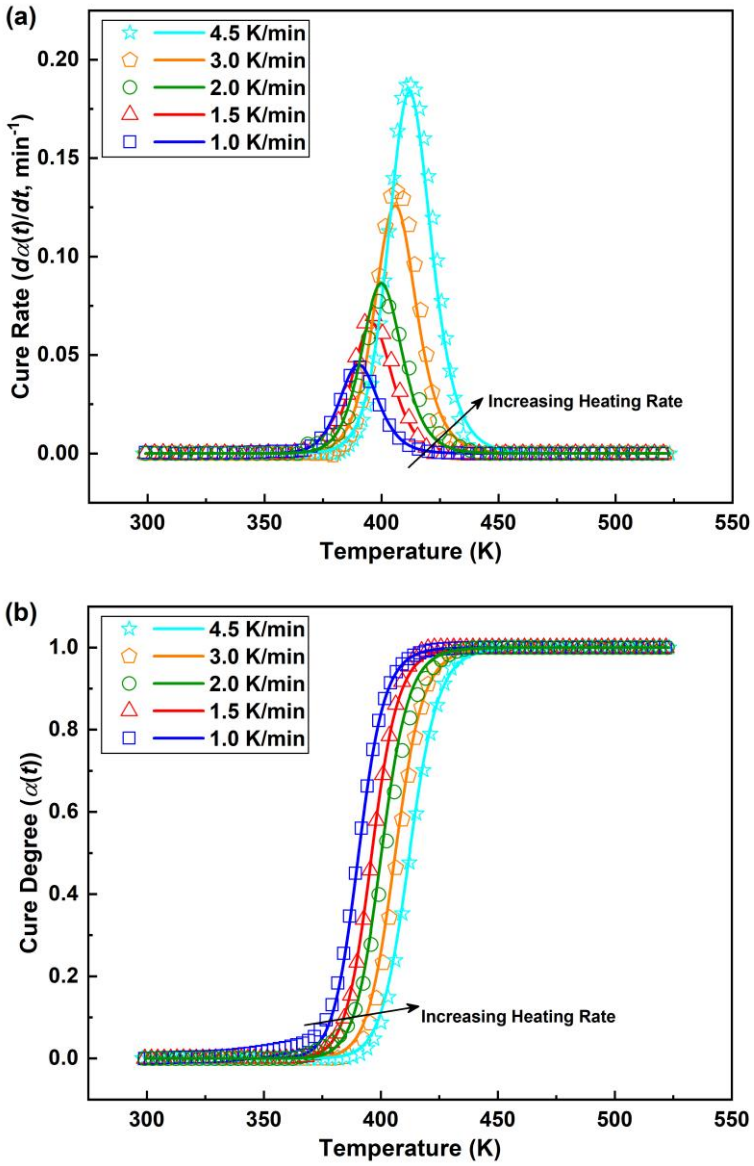

Fig. 3. (a) Cure rate ($\frac{d\alpha(t)}{dt}$) *versus* cure temperature; and (b) cure degree ($\alpha(t)$) *versus* cure temperature at different β (solid line: Sesták–Berggren model-predicted results; symbol: experimental results).

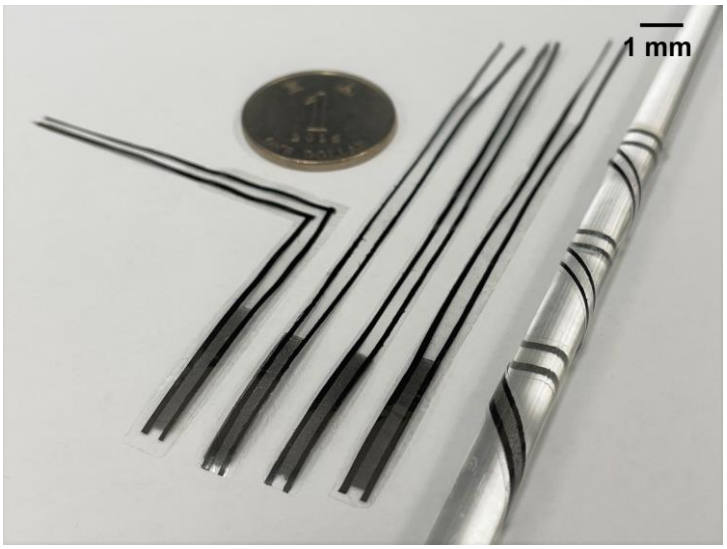

Fig. 4. Photograph of fabricated nanocomposite sensors, with a sensor wrapped on a thin rod (diameter: 8 mm) showing good flexibility of the sensor.

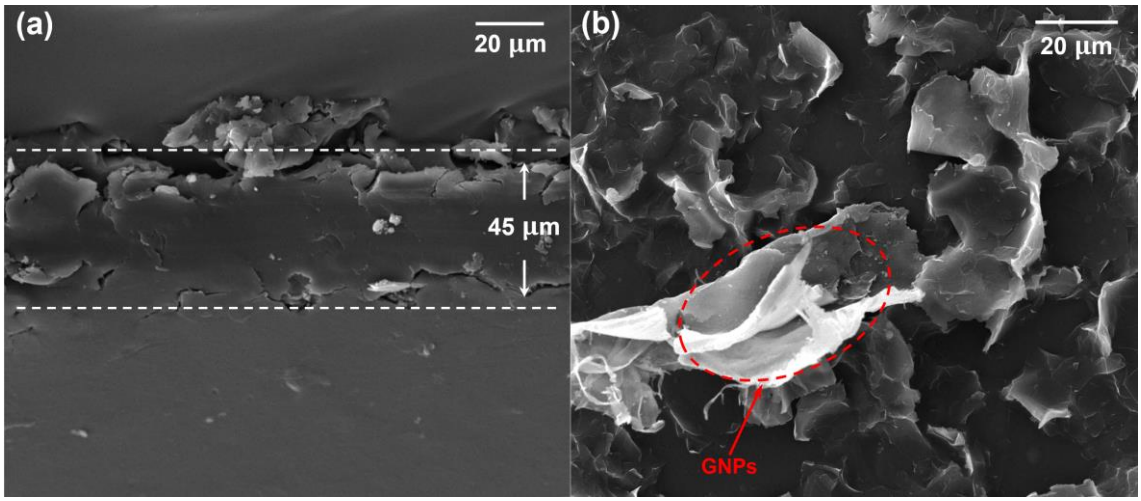

Fig. 5. SEM images of (a) an individual sensor, from which the thickness of sensor including its wires is measured to be ~45 µm); and (b) GNPs/PVP structure of the sensor.

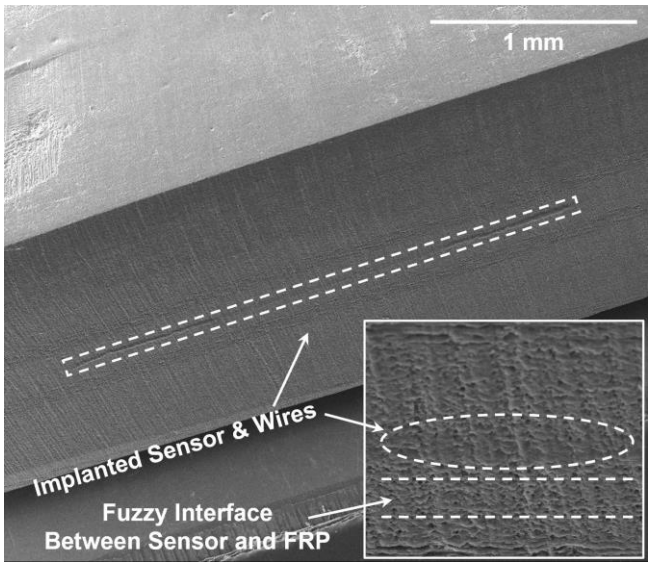

Fig. 6. Cross-sectional view of a FRP laminate with an implanted sensor including its CNT-film-made wires.

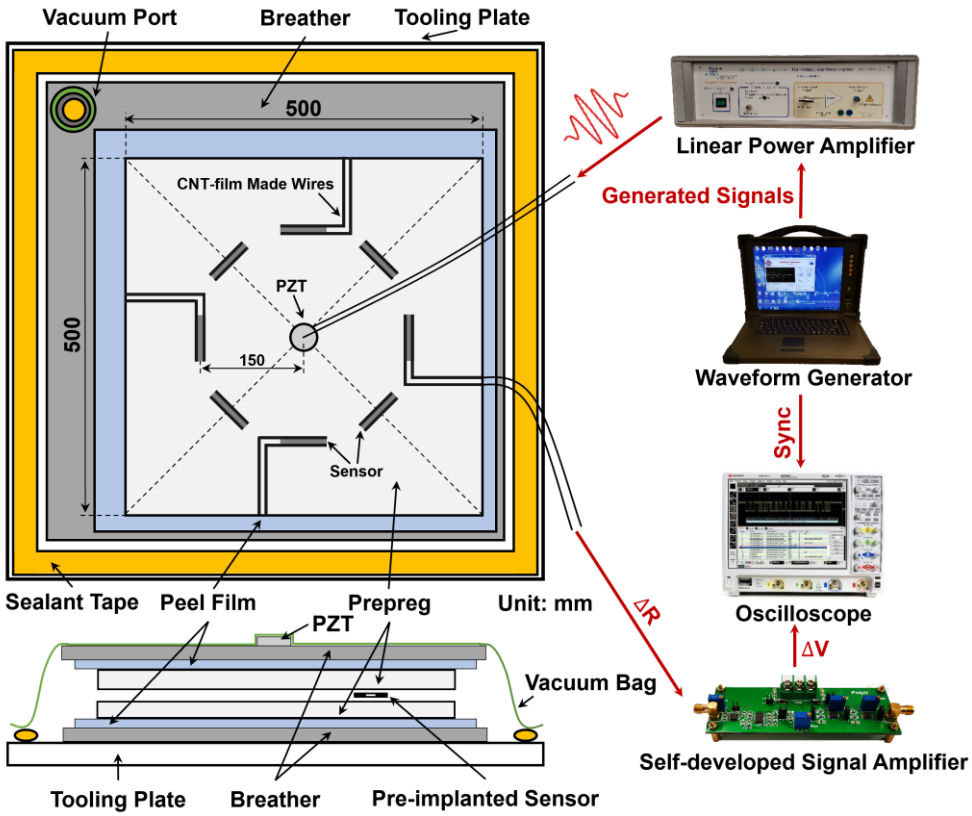

Fig. 7. Experimental set-up of GUW-based cure monitoring.

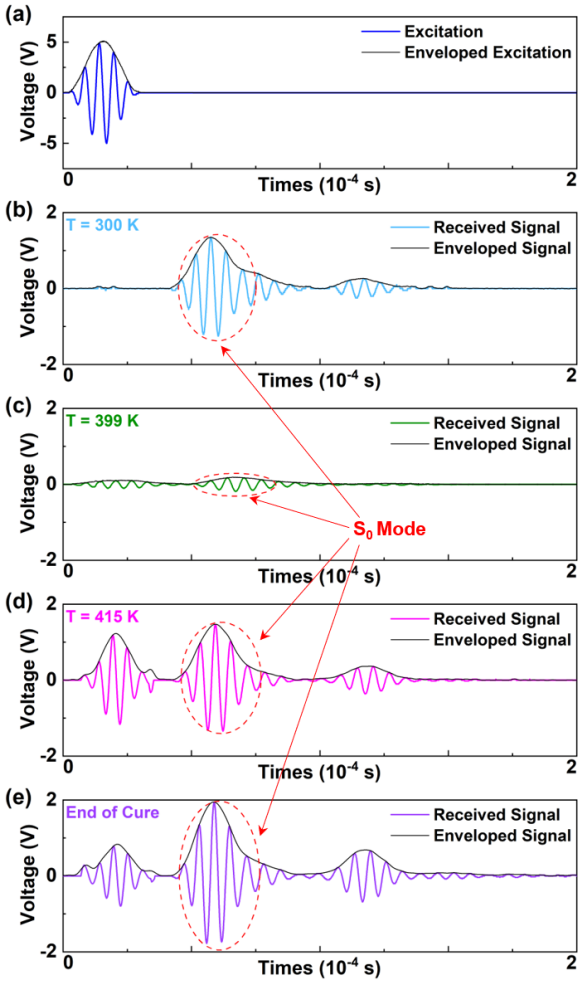

Fig. 8. Representative GUW signals captured by a pre-implanted sensor, along with wave energy envelopes, at different cure temperatures with the heating rate of 1.5 K/min.

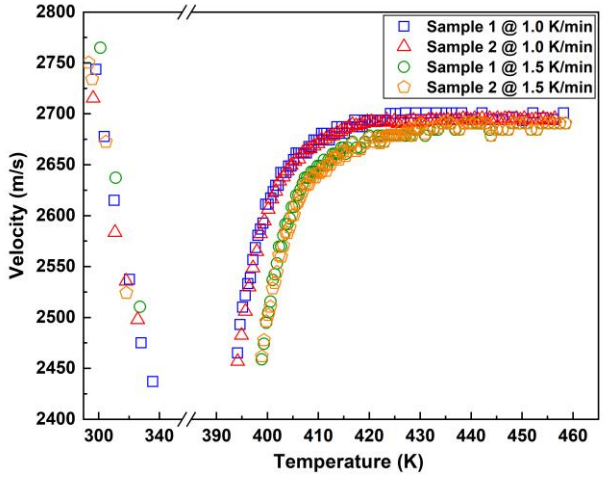

Fig. 9. Group velocity of S_0 wave mode at different cure temperatures, corresponding to different cure degrees.

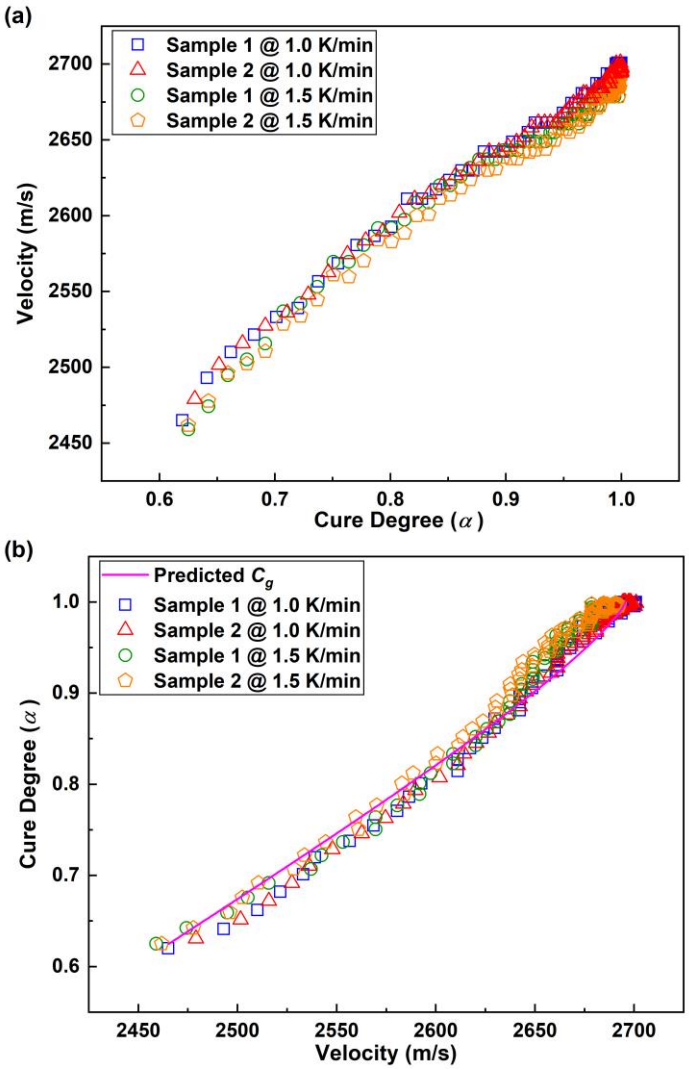

Fig. 10. (a) Measured C_g of GUWs *versus* cure degree of matrix; and (b) **Eq. (10)**-predicted correlation between cure degree of matrix and C_g of S_0 wave mode, compared with experimental results.

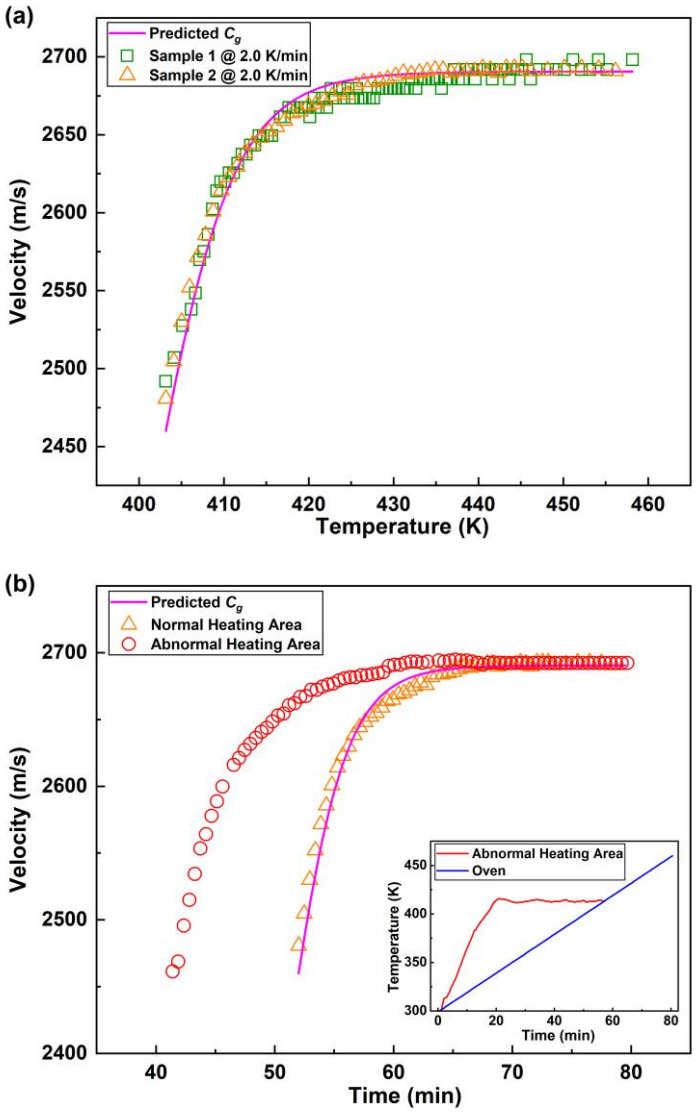

582

583

584

585 **Fig. 11.** (a) Group velocity of S_0 wave mode after gel point of matrix (at the heating rate of

586 2 K/min); and (b) comparison of C_g measured in normal and abnormal cure areas (solid

587 line: Sesták–Berggren model and **Eq. (10)**-predicted results; symbol: experimental results).

588

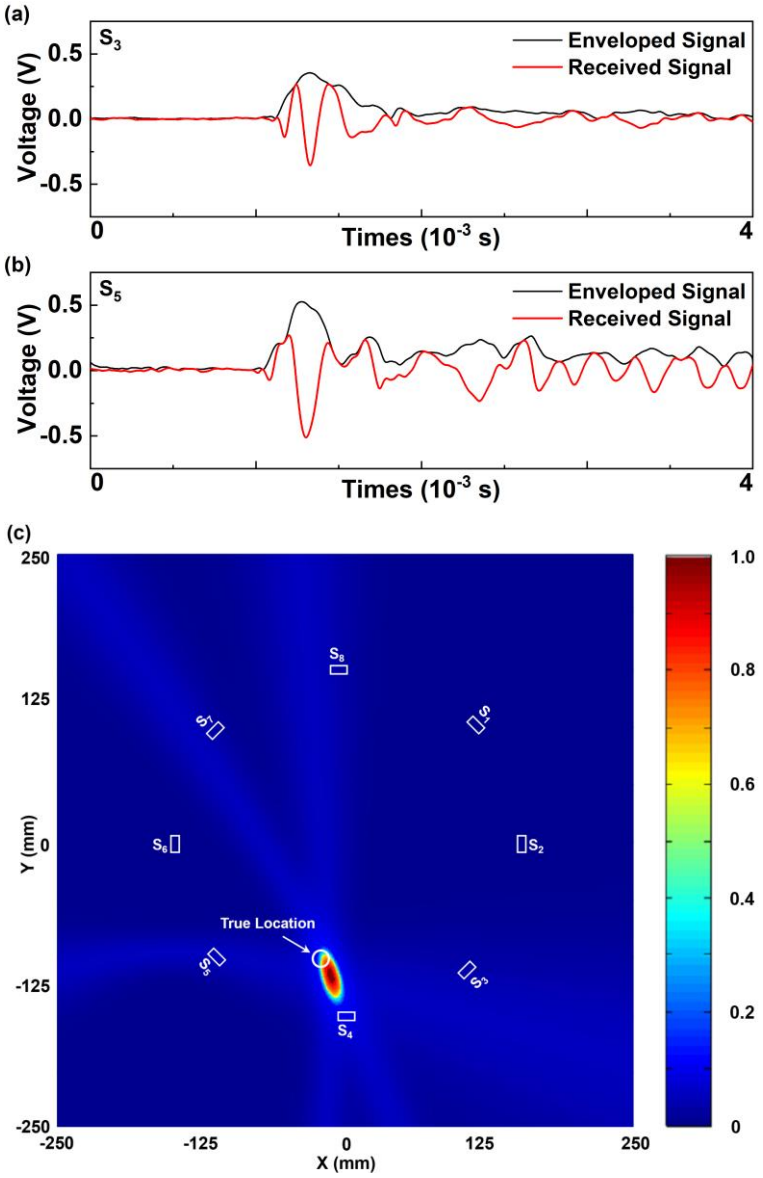

Fig. 12. (a, b) Representative raw and filtered AE signals acquired with S_3 and S_5; and (c) comparison between the real impact spot and the identified spot.

Table

Table 1. Determined parameters in Sesták–Berggren autocatalytic kinetic model.

E [kJ/mol]	ln$A$ [ln(min^{-1})]	m	n
86.26	24.87	0.60	1.43